

The Distribution of UV Radiation Field in the Molecular Clouds of Gould Belt

JIFENG XIA,^{1,2,3} NINGYU TANG,⁴ QIJUN ZHI,^{1,5} SIHAN JIAO,^{2,3} JINJIN XIE,⁶ GARY A. FULLER,^{7,8} PAUL F. GOLDSMITH,⁹ AND DI LI^{2,3}

¹*School of Physics and Electronic Science, Guizhou Normal University, Guiyang, 550025, China*

²*National Astronomical Observatories, Chinese Academy of Sciences, Beijing 100101, China*

³*University of Chinese Academy of Sciences, Beijing 100049, China*

⁴*Department of Physics, Anhui Normal University, Wuhu, Anhui 241002, China*

⁵*Guizhou Provincial Key Laboratory of Radio Astronomy and Data Processing, Guizhou Normal University, Guiyang 550001, China*

⁶*Shanghai Astronomical Observatory, CAS, Shanghai, 200030, China*

⁷*Jodrell Bank Centre for Astrophysics, Department of Physics & Astronomy, The University of Manchester, Manchester M13 9PL, United Kingdom*

⁸*I. Physikalisches Institut, University of Cologne, Zùlpicher Str. 77, 50937 Köln, Germany*

⁹*Jet Propulsion Laboratory, California Institute of Technology, 4800 Oak Grove Drive, Pasadena, CA 91109, USA*

ABSTRACT

The distribution of ultraviolet (UV) radiation field provides critical constraints on the physical environments of molecular clouds. Within 1 kpc of our solar system and fostering protostars of different masses, the giant molecular clouds in the Gould Belt present an excellent opportunity to resolve the UV field structure in star forming regions. We performed spectral energy distribution (SED) fitting of the archival data from the *Herschel* Gould Belt Survey (HGBS). Dust radiative transfer analysis with the DUSTY code were applied to 23 regions in 14 molecular complexes of the Gould Belt, resulting in the spatial distribution of radiation field in these regions. For 10 of 15 regions with independent measurements of star formation rate, their star formation rate and UV radiation intensity largely conform to a linear correlation found in previous studies.

Keywords: ISM:clouds—ISM:UV intensity—Dust—Radiative transfer

1. INTRODUCTION

Interstellar medium (ISM) is the cradle of star formation. Its evolution is strongly affected by the ultra-violet (UV) radiation. By ejecting electrons from dust grains and directly exciting atoms and molecules, UV photons ionize atoms, dissociate molecules and heat gases (e.g., Tielens & Hollenbach 1985; Ferrière 2001; Draine 2011). Kennicutt (1998) found a tight correlation between UV radiation and the star formation rate in galaxies. In Galactic studies, most previous studies focus on the distribution of UV radiation field of individual nearby regions (e.g. Liseau et al. 1999; Pineda et al. 2010).

Within 1 kpc of our Solar system, the Gould Belt containing a lot of molecular complexes provides an excellent opportunity to investigate the relationship between UV intensity and star formation rate under diverse environments (Ward-Thompson et al. 2007). Most molecular complexes of the Gould Belt harbor bright young OB stellar clusters or star-forming regions while the rest show little sign of star formation. For instance, Orion complex is a widely studied giant molecular region with abundant clustering OB stars and turbulent massive star formation (e.g., Lada et al. 1991; Tatematsu et al. 1998). Similar to Orion, Serpens/Aquila Rift is a rich complex with well-known massive star-forming regions, e.g., W40 HII region that contains embedded young high-mass stars (e.g., Kawamura et al. 1999). Although the Cepheus region contains an OB star (HD 200775 in Cep 1172), it has been generally considered as a low to intermediate mass star-forming region.

Lupus dark-cloud complex was found to be surrounded by about 70 T Tauri stars, with no indication of massive OB star inside (e.g., Hara et al. 1999). The Chamaeleon-Musca dark-cloud complex including Cha I, II, III, and the Musca dark lane, is a region with low-mass star formation (e.g., Cambrésy 1999; Mizuno et al. 2001). IC 5146 is a filamentary dark cloud with scattered low star formation activity (e.g., Dobashi et al. 1994). Pipe Nebula has been a primary example of little signs of disturbance from

star formation (e.g., Onishi et al. 1999). No star formation was found in the Polaris flare, a high-latitude translucent cloud (e.g., Heithausen & Thaddeus 1990).

Utilizing the Spectral and Photometric Imaging Receiver (SPIRE) and Photodetector Array Camera and Spectrometer (PACS) instruments on board the *Herschel*¹ Space Observatory, the *Herschel* Gould Belt Survey (HGBS) covered a substantial fraction of the Gould Belt. Specifically, images were taken at 250, 350, and 500 μm for regions with $A_V > 3$ mag with SPIRE and at 70 and 160 μm for those with $A_V > 6$ mag with PACS. This survey covers the following 14 molecular complexes: Aquila, Cepheus, Chamaleon, Corona Australis, IC 5146, Lupus, Musca, ρ Oph, Orion, Perseus, Pipe nebula, Polaris, Taurus, and Serpens.

The dust radiative transfer model, DUSTY (Ivezic & Elitzur 1997; Nenkova et al. 2000) accommodate different kinds of geometry and radiation parameters. Li et al. (2003) demonstrated the utilities of the DUSTY code to derive the UV intensity of the Orion clouds based on fitting the dust temperature data. We further develop the recipe and apply it to the full set of the HGBS data.

This paper is organized as follows. In Section 2, we introduce the data information of column density, dust temperature and star formation rate toward the HGBS molecular complexes. The DUSTY radiative transfer code and method for calculating the UV radiation intensity map are described in Section 3. Results and further discussions are presented in Section 4 and 5, respectively. The summary is in Section 6.

2. DATA

2.1. *Herschel* Dust Continuum Emission

Dust emission is almost always optically thin at (sub)millimetre wavelengths and can thus act as a surrogate tracer of the total (gas + dust) mass along the line of sight (LOS) (Roy et al. 2014). The HGBS took a census in the nearby (0.5 kpc) molecular cloud complexes for an extensive imaging survey of the densest portions of the Gould Belt, down to a 5σ column sensitivity $N_{H_2} \sim 10^{21} \text{ cm}^{-2}$ or $A_V \sim 1$ mag (André et al. 2010). We use the

HGBS data to generate the column density map of 23 molecular clouds that belongs to 14 molecular complexes of the Gould Belt.

The molecular clouds studied in this paper are Aquila M2 (André et al. 2010), Cep 1151, Cep 1172, Cep 1228, Cep 1241, Cep 1251 (Di Francesco et al. 2020), Cham I, Cham II, Cham III (Winston et al. 2012), (Alves de Oliveira et al. 2014), CrA NS (Bresnahan et al. 2018), IC 5146 (Arzoumanian et al. 2019), Lup I, Lup III, Lup IV (Rygl et al. 2013), Musca (Cox et al. 2016), ρ Oph Roy et al. (2014), Orion B (Könyves et al. 2020), Orion A (Jiao et al. accepted by SCPMA), Perseus (Pezzuto et al. 2012), Pipe (Peretto et al. 2012), Polaris (André et al. 2010), Taurus (Arzoumanian et al. 2019), and Serpens (Fiorellino et al. 2021).

2.2. Deriving Dust Temperature and Column Density Based on SED Fitting

The dust temperature and column density map toward 22 of 23 regions were downloaded from HGBS Archive². We obtained dust distribution and improved the image quality of the Orion A region, based on a novel image combination technique (Jiao et al. 2022, accepted).³ The procedure to derive the dust temperature and dust/gas column density images of Orion A is similar to that in Roy et al. (2014). Before performing any SED fitting, all images at multiple bands were convolved into beam size of $36''.3$ at 500 μm . We weighted the data points by the measured noise level in the least-squares fits. We adopted the dust opacity per unit mass at 300 μm of $0.1 \text{ cm}^2 \text{ g}^{-2}$ (Hildebrand 1983), and assumed a gas-to-dust mass ratio of 100. As modified black-body assumption, the flux density S_ν at a certain observing frequency ν is given by

$$S_\nu = \Omega_m B_\nu(T_d)(1 - e^{-\tau_\nu}), \quad (1)$$

where $B_\nu(T_d)$ is the Planck function at temperature T_d , Ω_m is the beam size. The total column density N of gas and dust can be approximated by

$$N = \frac{\tau_\nu}{\kappa_\nu \mu m_H}, \quad (2)$$

where the dust opacity $\kappa_\lambda = \kappa_{300\mu\text{m}}(\lambda/300\mu\text{m})^\beta$ (β was fixed to a constant value of 1.8), $\mu = 2.8$ is the mean molecular weight, m_H is the mass of a hydrogen atom. The grey-body dust temperature (T_d) thus calculated has ignored the dependence of dust temperature on grain size (Li et al. 1999), but has been shown to be within a couple of kelvins of the gas temperatures in well coupled regions (Goldsmith 2001; Li et al. 2013; Wang et al. 2020; Xie et al. 2021). The effect of scattering opacity (e.g., Liu 2019) can be safely ignored in the case given that focusing on >0.05 pc scale structures.

¹ *Herschel* is an European Space Agency (ESA) space observatory with science instruments provided by European-led Principal Investigator consortia and with important participation from NASA.

² The website of HGBS Archive: <http://www.herschel.fr/cea/gouldbelt/en/index.php>

³ The column density and dust temperature of Orion A was not published on the website of HGBS archive by 2022.

2.3. Star Formation Rates

The SFRs were determined through $SFR = N(\text{YSO})\langle M \rangle \tau^{-1}$, in which $N(\text{YSO})$ is the YSOs number in the molecular region, $\langle M \rangle$ is the mean mass of stars, and τ is the relevant evolution timescale.

The identification of YSOs requires careful discrimination against background stars and galaxies. Star-forming galaxies were the most problematic source of contaminants. A combination of color - color and color - magnitude diagrams of both Spitzer and 2MASS data were adopted to reject contaminants. The detailed descriptions of this process are shown in [Evans et al. \(2009\)](#). [Dunham et al. \(2013\)](#) provides a YSO catalog for Gould Belt clouds. To convert number of YSOs to mass of forming stars, [Evans et al. \(2014\)](#) adopted mean mass of stars $M_* = 0.5 M_\odot$, based on a fully sampled initial mass function ([Kroupa 2002](#)). The relevant timescales were derived by classifying YSOs into standard SED classes based on 2 to 24 μm data.

Table 1 lists the star formation rates ([Lada et al. 2010](#); [Evans et al. 2014](#)) we adopted in this paper.

Table 1. [

]Star formation rate of 15 molecular regions.

Cloud Name	RA (deg)	DEC (deg)	Distance ^a (pc)	Star Formation Rate ^a ($10^{-6} M_\odot \text{yr}^{-1}$)	Category ^b
Orion A	84.52	-7.03	423	715	I
Orion B	86.90	0.10	423	159	I
Serpens	278.78	4.6E-06	429	56	I
Perseus	53.92	31.53	250	150	I
ρ Oph	246.87	-24.21	125	79	I
Musca	186.81	-71.54	200	3	I
Lupus III	242.51	-39.08	200	17	II
Lupus IV	241.15	-42.07	150	3	II
Aquila	277.43	-2.78	260	322	II
IC 5146	327.19	47.49	460	24	II
Cham I	165.46	-77.40	150	20.5	II
Cham II	195.23	-77.41	178	6	II
Cham III	190.47	-79.82	150	1	II
Pipe	260.78	-26.40	145	5	II
Taurus	65.08	27.72	153	84	II

NOTE—The coordinates are determined by the data of HGBS.

^aThe values of distances and star formation rates are obtained from [Lada et al. \(2010\)](#) and [Evans et al. \(2014\)](#).

^bThe region with both OB stars and YSOs are defined as Category I; the region with YSOs only are defined as Category II.

3. METHOD

3.1. The DUSTY code

The public DUSTY code ([Ivezic & Elitzur 1997](#)) solves the radiative transfer problems through a fully scale-free method. By adopting this scaling method, the DUSTY code solves the spherically symmetric (1-D) problem with a single central radiation source and surrounding spherically symmetric dusty envelope, in which the radial dust density profile is arbitrary. Besides, a dusty plane-parallel slab with illumination from one or both sides at an arbitrary angle is available too.

This code utilizes the scaling properties to minimize the number of input parameters. Parameters describing the external radiation, dust and gas properties, cloud geometry are needed for inputs. For the case of spherical geometry, they include number, spectral shape and flux of the external source, chemical composition of dust, the lower and upper limit of dust optical depth, and density distribution of dust. For the case of slab geometry, an extra selection of source side is needed.

Once the input parameters are chosen, the DUSTY code outputs the value of dust temperature as a function of gas optical depth.

3.2. Parameter Setting in DUSTY Code

We adopted the slab geometry for our calculations. The incident angle between UV radiation and the slab, θ is treated as 0 degree, $\theta = 0^\circ$, indicating perpendicular UV radiation toward the slab. The selected radiation wavelength of $0.365 \mu\text{m}$ locates in the central wavelength of UV band. The dust sublimation temperature, which is the highest temperature the dust grains can exist, is chosen to be the common value of 1500 K. The value range of gas optical depth and dust temperature were chosen as $[0, 30]$ and $[0, 50]$ K, separately.

With the above selections, the UV radiation intensity, G_0 is the only parameter that determines the relationship between dust temperature and gas optical depth. As for the optional UV radiation flux received by one side of the slab, six sets of UV intensity ($G_0 = 1, 10, 31.6, 100, 316$, and 1000) compared to standard Habing field (e.g., [Hughes et al. 2017](#)) of $1.6 \times 10^{-6} \text{ W/m}^2$ were introduced for calculation.

3.3. Distribution of UV Intensity Field

In order to produce the spatial distribution of UV radiation field of the Gould Belt, we combined the DUSTY model calculations and the HGBS data.

The derived H_2 column density and dust temperature map of HGBS molecular complexes with pixel size of $3''$ were convolved and re-sampled with the beam size of $36.3''$ at $500 \mu\text{m}$. We are focusing on dense molecular regions, the contribution from atomic hydrogen can be ignored. Thus the H_2 column density was converted into gas optical depth at V band through the following equation ([Bohlin et al. 1978](#); [Greenberg 1968](#); [Rachford et al. 2009](#))

$$\tau_V = \frac{A_V}{1.086} = \frac{1.07 \times 10^{-21} N_{\text{H}_2}}{1.086}. \quad (3)$$

As an example, the derived relationship between T_{dust} and gas optical depth (τ_V) of all pixels for ρ Oph cloud can be found in Fig. 1. We obtained the UV intensity of each pixel by interpolating the results from observations with that from DUSTY model calculations. The spatial distribution of specific UV radiation field of each HGBS molecular complex can be derived.

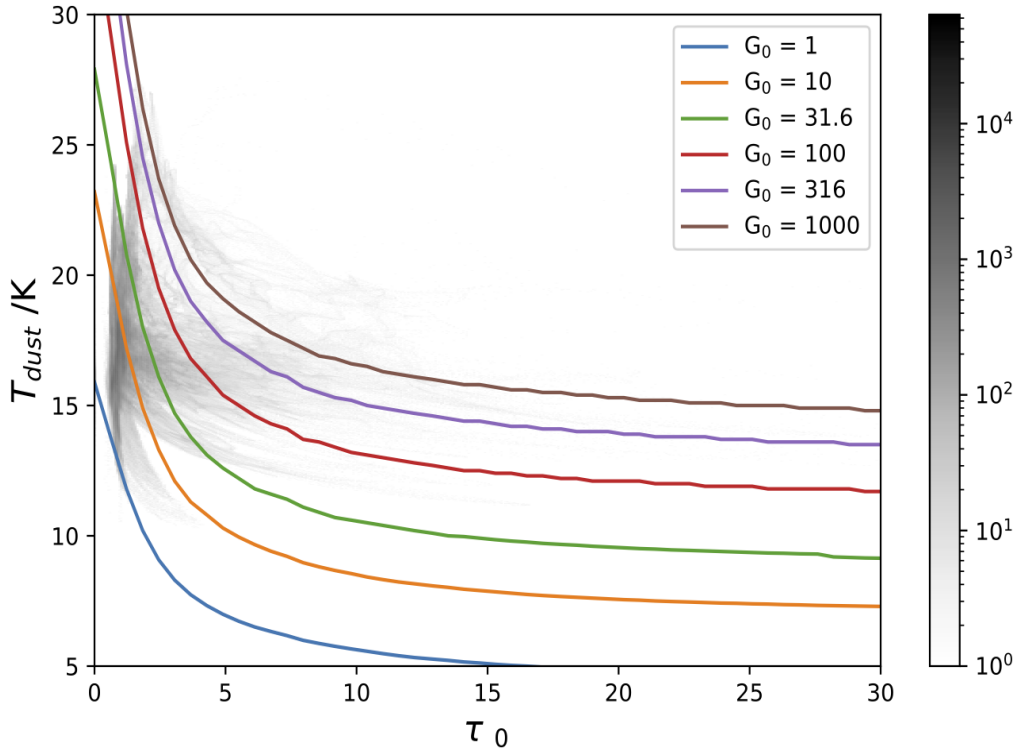


Figure 1. Relationship between dust temperature and optical depth. Results for the observed ρ Oph data are shown with grey point. Solid color lines represent model calculations from DUSTY code with different UV intensity value, G_0 .

4. RESULTS

After applying the procedures described in section 3, we obtained the UV intensity distribution of 23 regions in 14 molecular complexes of the Gould Belt.

4.1. Spatial Distribution of UV Intensity

As an example, We presented spatial distribution of selected UV intensity ($G_0 = 1, 10, 31.6, 100, 316, \text{ and } 1000$) for three molecular complexes: Orion (Category I), Aquila (Category II) and Polaris (Category III). Descriptions of the rest complexes are presented in Appendix.

4.1.1. Orion

Orion molecular complex is the most active star forming region within 500 pc (Megeath et al. 2012). Orion A and Orion B molecular clouds are covered by HGBS. Locating in Orion A, Orion Nebular cluster is a significant laboratory for understanding the initial mass function. The Orion B molecular cloud is one of the clouds scattered along the region named Orion-Eridanus superbubble, which was created by supernova explosions (Könyves et al. 2020). The Orion B cloud is ~ 423 pc away and covers an area of $\sim 6.8 \times 8.6 \text{ deg}^2$ (Evans et al. 2014). The total mass of these two molecular clouds exceed $2 \times 10^5 M_\odot$ (Megeath et al. 2012).

As shown in Fig. 2, the UV intensity of these two regions show tight correlation with the OB stars.

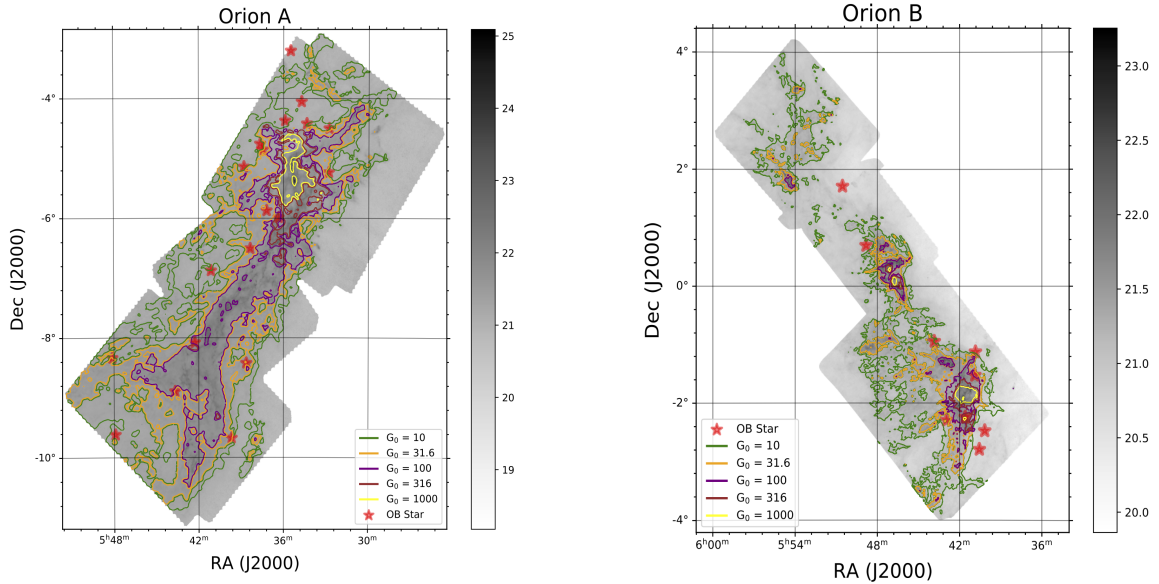


Figure 2. Contours of UV intensity overlaid on H_2 column density map of the Orion A (left panel) and Orion B (right panel) region. The column density $N(H_2)$ are shown with $\log_{10} N(H_2)$ value. The red star implies the location of OB star in this region.

4.1.2. Aquila

The Aquila field is a very active star-forming region at a distance of about 260 pc (Evans et al. 2014). With size of ~ 7.56 pc, the mass of this molecular complex is about $24446 M_\odot$, of which two-thirds are composed of dense cores (Evans et al. 2014). The existence of dense cloud leads to highest level of background cloud emission in HGBS. Cluster of YSOs but no OB stars were detected in this region. The number of YSOs in this region exceeds 1000.

As shown in Figure 3, the intensity of the radiation field distribution varies from $G_0=1$ to $G_0=1000$. We found a certain correlation between the spatial distribution of YSOs and UV radiation field. The possible reason responsible for this is discussed in section 5.

4.1.3. Polaris

The Polaris Flare has a distance of about 352 pc and total mass of about $5500 M_\odot$ (Zucker et al. 2019). It is a high-latitude translucent cloud with little or no obvious star formation activity. It is expected to have the lowest level of background cloud

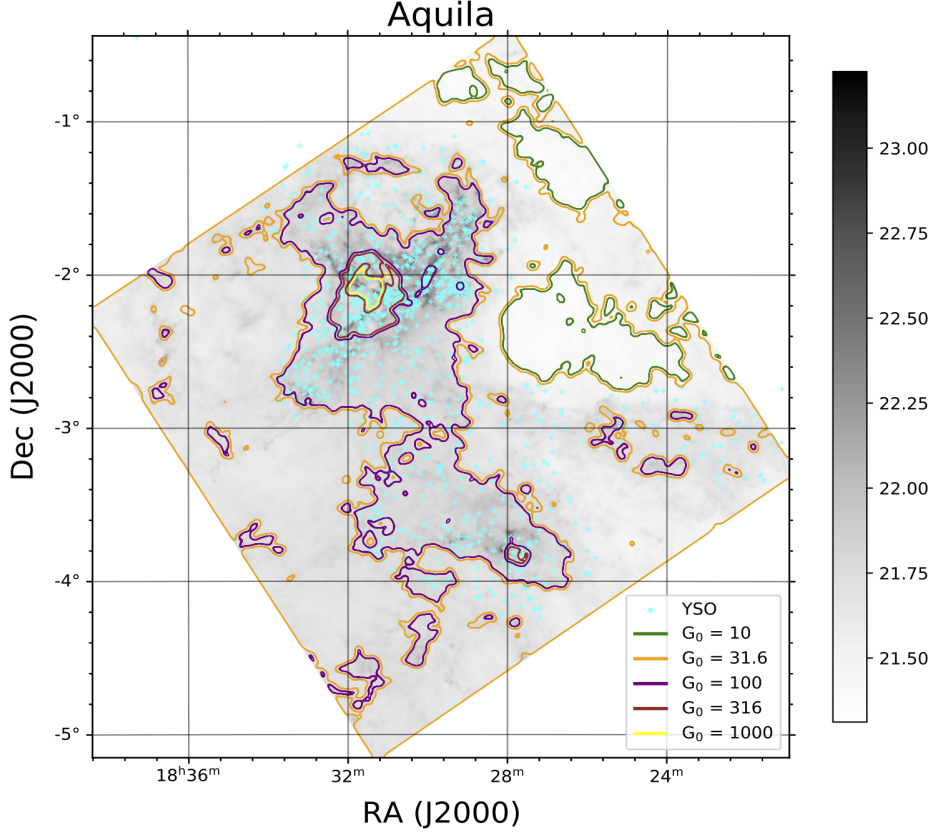


Figure 3. Contours of UV intensity overlaid on H_2 column density map of the Aquila molecular complex. The column density $N(H_2)$ are shown with $\log_{10}N(H_2)$ value. The cyan dots represent the locations of YSOs.

emission (Heithausen & Thaddeus 1990). No OB stars nor YSOs were detected in this region. As shown in Fig.4, the UV intensity G_0 of almost all region is smaller than 10.

4.2. UV Intensity vs $N(H_2)$

We presented a statistical result between UV intensity G_0 and peak H_2 column density $N(H_2)$ of each molecular cloud in Fig. 5. The correlation between G_0 and $N(H_2)$ can be fitted with a linear function of

$$\log(G_0) = (0.62 \pm 0.12)\log(N(H_2)) - (11.56 \pm 2.87) , \quad (4)$$

for all complexes. It becomes

$$\log(G_0) = (0.94 \pm 0.17)\log(N(H_2)) - (18.76 \pm 3.91) , \quad (5)$$

when Orion A was not included.

5. DISCUSSION

In this paper, we obtained the distribution of UV radiation field toward 23 regions of 14 molecular complexes in Gould Belt through dust radiative analysis.

5.1. Uncertainty Analysis

The main assumption of such analysis is that the heating of dust was mainly due to UV radiation from massive stars. This has been demonstrated to be valid in the presence of massive stars, particularly, OB clusters (e.g., Li et al. 1999, 2003). In more

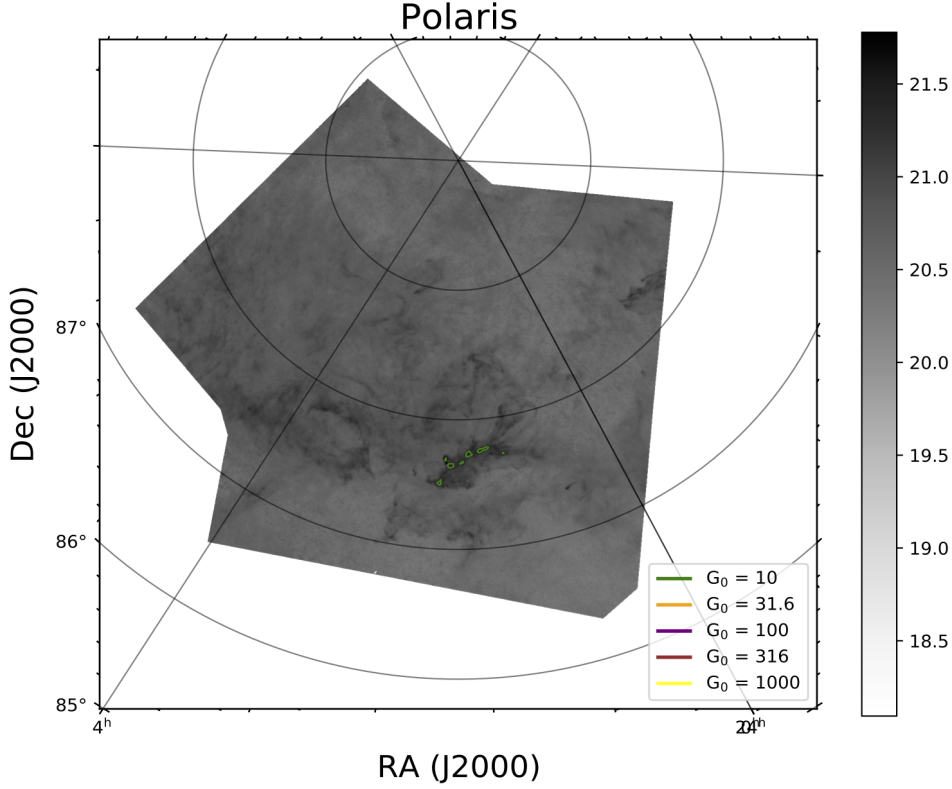


Figure 4. Contours of UV intensity overlaid on H_2 column density map of the Polaris region. The labels of the figure are the same as that in Fig. 3. No YSOs or OB star were found in this region.

quiescent regions, however, dynamic feedback through outflows and bubbles from low-mass stars have proven to be capable of sustaining the turbulence in, e.g. Taurus (Li et al. 2015), thus presumably may result in some dust heating. However, even suppose the gas and dust are closely coupled, there is no sign of elevated temperatures close to low-mass YSOs in Taurus (Goldsmith et al. 2008). We thus consider the heating of dust from low-mass YSOs to be minor.

In testing the model, we find that the incident angle affect more the absolute value of the derived UV field, rather than its distribution. To obtain robust results for the Gould belt sample in a systematic way, we set the incident angle to zero. Further investigation of the individual radiation geometry is warranted.

5.2. Compare with Star Formation Rate

We obtain the total UV fluxes in Aquila, Cham I, Cham II, Cham III, IC5146, Lupus III, Lupus IV, Serpens, Musca, ρ Oph, Orion A, Orion B, Pipe, Perseus, and Taurus by adding up the DUSTY outputs for each region and compare them with the star formation rate in Lada et al. (2010); Evans et al. (2014).

UV emission is a direct tracer of the recent SFR since it traces the photospheric emission of young stars. The investigation of SFR of extragalaxies has been revolutionized with the observations of GALEX telescope (Martin et al. 2005). By combining the UV data and Initial Mass Function (IMF), the relationship between SFR and UV luminosity (Hao et al. 2011; Kennicutt & Evans 2012) can be described as

$$\log(\dot{M}_{\odot}) = \log(L_{\nu}) - \log(C) , \quad (6)$$

where \dot{M}_{\odot} is SFR in unit of $10^{-6} M_{\odot} \text{ year}^{-1}$, $L_{\nu}(\text{FUV})$ is FUV luminosity in unit of ergs s^{-1} , $\log(C) = 43.35$ is conversion constant.

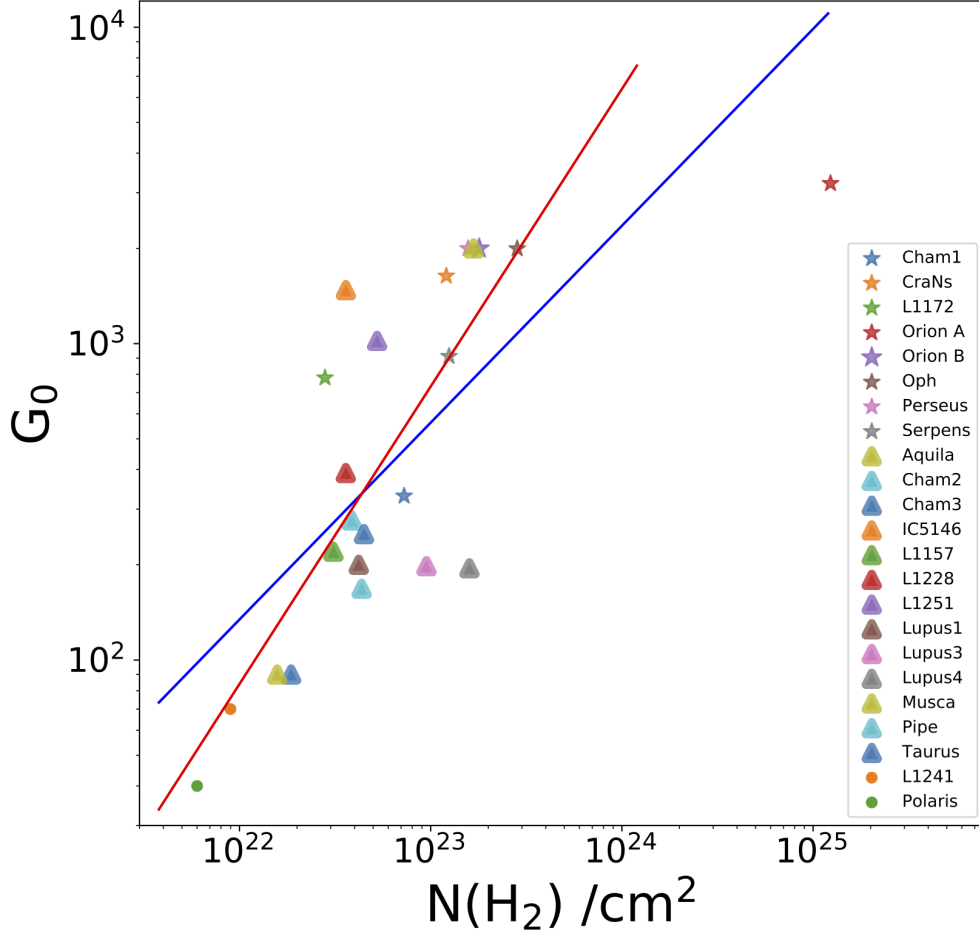


Figure 5. The relationship between UV intensity G_0 and peak H_2 column density $N(H_2)$. Filled star, triangle, and circle represent category I, II and III, respectively. The blue solid line represents linear fit of all clouds. The red solid line represents linear fit when Orion A is excluded.

The relationship between UV intensity and SFR for 15 molecular regions of Gould Belt is presented in Fig. 6. The blue line denotes the correlation between UV flux by OB stars and star formation rate. The correlation conforms to the general expectation. Regions with prominent OB clusters tend to be more consistent with the expectation. The scatter is bigger where there is no OB star. Different regions in the same molecular cloud tend to have similar UV fields, but different star formation rate. The less massive YSOs seem to have little effect on the UV distribution.

6. SUMMARY

By interpreting dust continuum data through radiative transfer analysis, we obtained UV intensity distribution toward 23 molecular regions in the Gould Belt. The main results of this study are summarized as follows,

1. The UV intensity G_0 of molecular clouds ranges from 1 to over 1000, relative to the Habing interstellar field.
2. The UV distribution in the majority of the molecular regions shows a tight correlation with that of OB stars and/or YSOs.
3. The UV intensity of 10 molecular regions conforms to an expected linear correlation with the SFR.

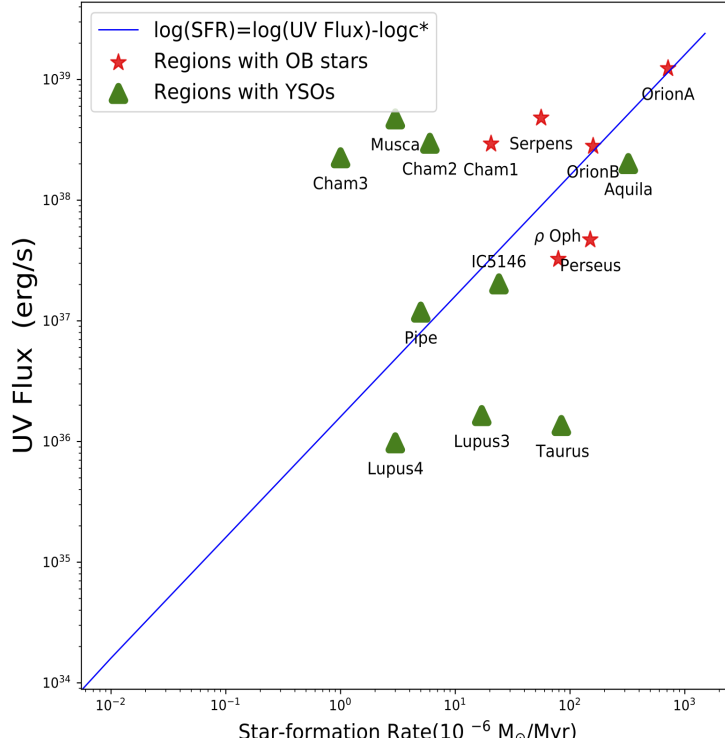


Figure 6. The relationship between total UV flux and star formation rate in 15 molecular clouds including Lupus, Corona Australis, Pipe, Musca, ρ Oph, Perseus, Aquila, Orion A, Orion B, Serpens, IC 5146, Chamaleon. The blue line indicates the formula of equation 6. Regions with massive OB stars fit the blue line better than regions with YSOs.

ACKNOWLEDGMENTS

This work is supported by the National Natural Science Foundation of China (NSFC) grant No. 11988101, No. 11725313, No. 11721303, No. U1731238, the International Partnership Program of Chinese Academy of Sciences grant No.114A11KYSB20160008, the National Key R&D Program of China No. 2016YFA0400702, the Guizhou Provincial Science and Technology Foundation (Nos. [2016]4008, [2017]5726-37,), the Foundation of Guizhou Provincial Education Department (No. KY (2020) 003). This research was carried out in part at the Jet Propulsion Laboratory, California Institute of Technology, under contract with the National Aeronautics and Space Administration. This research made use of APLPY, an open-source plotting package for Python(?).

REFERENCES

- | | |
|-----------------------------------------------------------------------------------------------------------------------------------------|-----------------------------------------------------------------------------------------------------------|
| Kirsanova, M. S., Punanova, A. F., Semenov, D. A., et al. 2021, MNRAS, 507, 3810. doi:10.1093/mnras/stab2361 | Wang, S., Ren, Z., Li, D., et al. 2020, MNRAS, 499, 4432. doi:10.1093/mnras/staa3059 |
| Xie, J., Fuller, G. A., Li, D., et al. 2021, Science China Physics, Mechanics, and Astronomy, 64, 279511. doi:10.1007/s11433-021-1695-0 | Di Francesco, J., Keown, J., Fallscheer, C., et al. 2020, ApJ, 904, 172. doi:10.3847/1538-4357/abc016 |
| Hahlin, A., Kochukhov, O., Alecian, E., et al. 2021, A&A, 650, A197. doi:10.1051/0004-6361/202140832 | Kirsanova, M. S., Boley, P. A., Moiseev, A. V., et al. 2020, MNRAS, 497, 1050. doi:10.1093/mnras/staa2004 |
| Fiorellino, E., Elia, D., André, P., et al. 2021, MNRAS, 500, 4257. doi:10.1093/mnras/staa3420 | Könyves, V., André, P., Arzoumanian, D., et al. 2020, A&A, 635, A34. doi:10.1051/0004-6361/201834753 |
| Pezzuto, S., Benedettini, M., Di Francesco, J., et al. 2021, A&A, 645, A55. doi:10.1051/0004-6361/201936534 | Liu, M., Li, D., Krčo, M., et al. 2019, ApJ, 885, 124. doi:10.3847/1538-4357/ab4880 |

- Zucker, C., Speagle, J. S., Schlafly, E. F., et al. 2019, *ApJ*, 879, 125. doi:10.3847/1538-4357/ab2388
- Liu, H. B. 2019, *ApJL*, 877, L22. doi:10.3847/2041-8213/ab1f8e
- Arzoumanian, D., André, P., Könyves, V., et al. 2019, *A&A*, 621, A42. doi:10.1051/0004-6361/201832725
- Bresnahan, D., Ward-Thompson, D., Kirk, J. M., et al. 2018, *A&A*, 615, A125. doi:10.1051/0004-6361/201730515
- Hughes, T. M., Ibar, E., Villanueva, V., et al. 2017, *A&A*, 602, A49. doi:10.1051/0004-6361/201629588
- Cox, N. L. J., Arzoumanian, D., André, P., et al. 2016, *A&A*, 590, A110. doi:10.1051/0004-6361/201527068
- Li, H., Li, D., Qian, L., et al. 2015, *ApJS*, 219, 20. doi:10.1088/0067-0049/219/2/20
- Alves de Oliveira, C., Schneider, N., Merín, B., et al. 2014, *A&A*, 568, A98. doi:10.1051/0004-6361/201423504
- Evans, N. J., Heiderman, A., & Vutisalchavakul, N. 2014, *ApJ*, 782, 114. doi:10.1088/0004-637X/782/2/114
- Roy, A., André, P., Palmeirim, P., et al. 2014, *A&A*, 562, A138. doi:10.1051/0004-6361/201322236
- Kirk, J. M., Ward-Thompson, D., Palmeirim, P., et al. 2013, *MNRAS*, 432, 1424. doi:10.1093/mnras/stt561
- Li, D., Kauffmann, J., Zhang, Q., et al. 2013, *ApJL*, 768, L5. doi:10.1088/2041-8205/768/1/L5
- Dunham, M. M., Arce, H. G., Allen, L. E., et al. 2013, *AJ*, 145, 94. doi:10.1088/0004-6256/145/4/94
- Palmeirim, P., André, P., Kirk, J., et al. 2013, *A&A*, 550, A38. doi:10.1051/0004-6361/201220500
- Roy, A., Martin, P. G., Polychroni, D., et al. 2013, *ApJ*, 763, 55. doi:10.1088/0004-637X/763/1/55
- Rygl, K. L. J., Benedettini, M., Schisano, E., et al. 2013, *A&A*, 549, L1. doi:10.1051/0004-6361/201219511
- Megeath, S. T., Gutermuth, R., Muzerolle, J., et al. 2012, *AJ*, 144, 192. doi:10.1088/0004-6256/144/6/192
- Pezzuto, S., Elia, D., Schisano, E., et al. 2012, *A&A*, 547, A54. doi:10.1051/0004-6361/201219501
- Winston, E., Cox, N. L. J., Prusti, T., et al. 2012, *A&A*, 545, A145. doi:10.1051/0004-6361/201118665
- Li, D. & Goldsmith, P. F. 2012, *ApJ*, 756, 12. doi:10.1088/0004-637X/756/1/12
- Kennicutt, R. C. & Evans, N. J. 2012, *ARA&A*, 50, 531. doi:10.1146/annurev-astro-081811-125610
- Kóspál, Á., Prusti, T., Cox, N. L. J., et al. 2012, *A&A*, 541, A71. doi:10.1051/0004-6361/201218823
- Peretto, N., André, P., Könyves, V., et al. 2012, *A&A*, 541, A63. doi:10.1051/0004-6361/201118663
- Hao, C.-N., Kennicutt, R. C., Johnson, B. D., et al. 2011, *Galaxy Evolution: Infrared to Millimeter Wavelength Perspective*, 446, 63
- Draine, B. T. 2011, *Physics of the Interstellar and Intergalactic Medium* by Bruce T. Draine. Princeton University Press, 2011. ISBN: 978-0-691-12214-4
- Lada, C. J., Lombardi, M., & Alves, J. F. 2010, *ApJ*, 724, 687. doi:10.1088/0004-637X/724/1/687
- Pineda, J. L., Velusamy, T., Langer, W. D., et al. 2010, *A&A*, 521, L19. doi:10.1051/0004-6361/201015089
- Pilbratt, G. L., Riedinger, J. R., Passvogel, T., et al. 2010, *A&A*, 518, L1. doi:10.1051/0004-6361/201014759
- André, P., Men'shchikov, A., Bontemps, S., et al. 2010, *A&A*, 518, L102. doi:10.1051/0004-6361/201014666
- Men'shchikov, A., André, P., Didelon, P., et al. 2010, *A&A*, 518, L103. doi:10.1051/0004-6361/201014668
- Forbrich, J., Lada, C. J., Muench, A. A., et al. 2009, *ApJ*, 704, 292. doi:10.1088/0004-637X/704/1/292
- Evans, N. J., Dunham, M. M., Jørgensen, J. K., et al. 2009, *ApJS*, 181, 321. doi:10.1088/0067-0049/181/2/321
- Rachford, B. L., Snow, T. P., Destree, J. D., et al. 2009, *ApJS*, 180, 125. doi:10.1088/0067-0049/180/1/125
- Goldsmith, P. F., Heyer, M., Narayanan, G., et al. 2008, *ApJ*, 680, 428. doi:10.1086/587166
- Gutermuth, R. A., Bourke, T. L., Allen, L. E., et al. 2008, *ApJL*, 673, L151. doi:10.1086/528710
- Ward-Thompson, D., Di Francesco, J., Hatchell, J., et al. 2007, *PASP*, 119, 855. doi:10.1086/521277
- Alves, F. O. & Franco, G. A. P. 2007, *A&A*, 470, 597. doi:10.1051/0004-6361:20066759
- Lombardi, M., Alves, J., & Lada, C. J. 2006, *A&A*, 454, 781. doi:10.1051/0004-6361:20042474
- Martin, D. C., Fanon, J., Schiminovich, D., et al. 2005, *ApJL*, 619, L1. doi:10.1086/426387
- Li, D., Goldsmith, P. F., & Menten, K. 2003, *ApJ*, 587, 262. doi:10.1086/368078
- Heithausen, A., Bertoldi, F., & Bensch, F. 2002, *A&A*, 383, 591. doi:10.1051/0004-6361:20011806
- Kroupa, P. 2002, *Science*, 295, 82. doi:10.1126/science.1067524
- Mizuno, A., Yamaguchi, R., Tachihara, K., et al. 2001, *PASJ*, 53, 1071. doi:10.1093/pasj/53.6.1071
- Ferrière, K. M. 2001, *Reviews of Modern Physics*, 73, 1031. doi:10.1103/RevModPhys.73.1031
- Goldsmith, P. F. 2001, *ApJ*, 557, 736. doi:10.1086/322255
- Nenkova, M., Ivezić, Ž., & Elitzur, M. 2000, *Thermal Emission Spectroscopy and Analysis of Dust, Disks, and Regoliths*, 196, 77
- Onishi, T., Kawamura, A., Abe, R., et al. 1999, *PASJ*, 51, 871. doi:10.1093/pasj/51.6.871
- Kawamura, A., Onishi, T., Mizuno, A., et al. 1999, *PASJ*, 51, 851. doi:10.1093/pasj/51.6.851
- Hara, A., Tachihara, K., Mizuno, A., et al. 1999, *PASJ*, 51, 895. doi:10.1093/pasj/51.6.895

- Li, D., Goldsmith, P. F., & Xie, T. 1999, *ApJ*, 522, 897.
doi:10.1086/307668
- Meurer, G. R., Heckman, T. M., & Calzetti, D. 1999, *ApJ*, 521, 64.
doi:10.1086/307523
- Cambr  sy, L. 1999, *A&A*, 345, 965
- Liseau, R., White, G. J., Larsson, B., et al. 1999, *A&A*, 344, 342
- de Zeeuw, P. T., Hoogerwerf, R., de Bruijne, J. H. J., et al. 1999, *AJ*, 117, 354. doi:10.1086/300682
- Tatematsu, K., Umemoto, T., Heyer, M. H., et al. 1998, *ApJS*, 118, 517. doi:10.1086/313143
- Kennicutt, R. C. 1998, *ARA&A*, 36, 189.
doi:10.1146/annurev.astro.36.1.189
- Ivezic, Z. & Elitzur, M. 1997, *MNRAS*, 287, 799.
doi:10.1093/mnras/287.4.799
- Haardt, F. & Madau, P. 1996, *ApJ*, 461, 20. doi:10.1086/177035
- Dobashi, K., Bernard, J.-P., Yonekura, Y., et al. 1994, *ApJS*, 95, 419. doi:10.1086/192106
- Vilas-Boas, J. W. S., Myers, P. C., & Fuller, G. A. 1994, *ApJ*, 433, 96. doi:10.1086/174628
- Stacey, G. J., Jaffe, D. T., Geis, N., et al. 1993, *ApJ*, 404, 219.
doi:10.1086/172270
- Wilking, B. A. 1992, *Low Mass Star Formation in Southern Molecular Clouds*, 159
- Franco, G. A. P. 1991, *A&A*, 251, 581
- Lada, E. A., Bally, J., & Stark, A. A. 1991, *ApJ*, 368, 432.
doi:10.1086/169708
- Heithausen, A. & Thaddeus, P. 1990, *ApJL*, 353, L49.
doi:10.1086/185705
- Loren, R. B. 1989, *ApJ*, 338, 902. doi:10.1086/167244
- Tielens, A. G. G. M. & Hollenbach, D. 1985, *ApJ*, 291, 722.
doi:10.1086/163111
- Wilking, B. A. & Lada, C. J. 1983, *ApJ*, 274, 698.
doi:10.1086/161482
- Hildebrand, R. H. 1983, *QJRAS*, 24, 267
- Bohlin, R. C., Savage, B. D., & Drake, J. F. 1978, *ApJ*, 224, 132.
doi:10.1086/156357
- Worden, S. P. & Grasdalen, G. L. 1974, *A&A*, 34, 37
- Greenberg, J. M. 1968, *Nebulae and Interstellar Matter*, 221

APPENDIX

A. UV DISTRIBUTION OF THE GOULD BELT COMPLEXES

A.1. *Cepheus*

Located at a high declination, the Cepheus molecular complex includes many regions that have loose association with compact dark clouds. HGBS contains 5 regions in Cepheus molecular complex, Cep 1157 (also known as L1157, the same below), Cep 1172, Cep 1228, Cep 1241 and Cep 1251. The distance of the five regions are considered to be 200-300 pc. The masses of L1157, L1172, L1228, L1241, L1251 are $1400 M_{\odot}$, $1900 M_{\odot}$, $1600 M_{\odot}$, $3200 M_{\odot}$ and $1800 M_{\odot}$ (Di Francesco et al. 2020). L1172 is the host of the bright NGC 7023 reflection nebula, which contains the bright B star, HD200775 in these five regions. L1241 and L1251 lie within the Cepheus Flare Shell. L1241 is the only one region without YSOs nor OB star. Some YSOs are found in L1251. The L1228 locates at the edge of the Cepheus Flare Shell, while L1157 and L1172 locate outside to the Cepheus Flare Shell.

The radiation field distribution of these five regions are quite different depending on the existence of massive stars and YSOs. As shown in Fig.8, the UV intensity of L1172 around HD 200775 can exceed $1000 G_0$. For the L1157 (Fig. 7), L1228 (Fig.8) and L1251 (Fig.11) regions, obvious higher UV intensity can be found around the YSOs. The UV intensity in L1241 is smaller than $31.6 G_0$ while there are no massive stars nor YSOs in this region.

A.2. *Chamaleon*

Chamaleon is a nearby low-mass star-forming region containing Cham I, Cham II and Cham III. The distance from the regions in Chamaleon is about 150 pc (Evans et al. 2014). The entire Cham I region covers an area about 5 deg^2 , containing about 200 known low-mass YSOs, making it one of the closest and richest star-forming regions. The total mass of this cloud is about $482 M_{\odot}$, one third of which are dense gas (Evans et al. 2014). Though there is abundant low-mass YSOs in Cham I, there is only one B star: HD 97300 in the northern part of the cloud (Winston et al. 2012).

Cham II region contains a smaller number(~ 60) of YSOs compared to the Cha I region. The size of Cham II is about 1.78 pc. The total mass of Cham II is about $637 M_{\odot}$ while one tens is dense gas. As the largest cloud of the three regions with a total mass of $746 M_{\odot}$, Cham III contain little dense gas and only a few YSOs(Alves de Oliveira et al. 2014).

Due to the differences in containing YSOs and dense gas, the UV intensity distribution of Cham I, Cham II and Cham III are expected to vary significantly. As shown in Fig. 12, 13, and 14, the maximum UV intensity value decrease from Cham I to Cham III, which is proportional with the existence of OB stars.

A.3. *CraNS*

With distance of around 130 pc and being out of the Galactic plane, the CraNS (Corona Australis) molecular cloud is a low-mass star-forming region. The total mass of this region is about $279 M_{\odot}$, half of which is dense gas (Evans et al. 2014). There is an OB star($V^* \text{ R CrA}$) and a cluster of YSOs in this region (Bresnahan et al. 2018). As shown in Fig. 15, the derived UV intensity G_0 around the OB star can exceed 1000.

A.4. *IC 5146*

With a distance of ~ 460 pc, IC 5146 region covers an area of $\sim 3.1 \times 2.5 \text{ deg}^2$. The total mass of this cloud is about $3.7 \times 10^3 M_{\odot}$ (Arzoumanian et al. 2019). There is little dense gas nor OB star in this region (Evans et al. 2014). Abundant YSOs exist in this region. We present UV intensity distribution for IC 5146 in Fig. 16. The UV intensity G_0 can reach 31.6 around the YSOs.

A.5. *Lupus*

The distance of Lupus molecular complex is about 189 pc (Zucker et al. 2019). The HGBS surveyed three clouds in this complex: Lupus I, Lupus III and Lupus IV cloud. Among the three clouds, the Lupus I cloud is the youngest one. The mass of Lupus I is about $512 M_{\odot}$. Lup III is the most evolved cloud with mass of $\sim 912 M_{\odot}$. Lupus IV cloud has a middle property between Lupus I and III cloud. The mass of dense gas in Lupus IV cloud is $50 M_{\odot}$, accounting for about one quarter of the cloud mass (Evans et al. 2014). These three clouds contain YSOs but there are no massive stars inside.

As shown in Fig 17, 18 and 19, the UV intensity distribution correlate with the existences of YSOs.

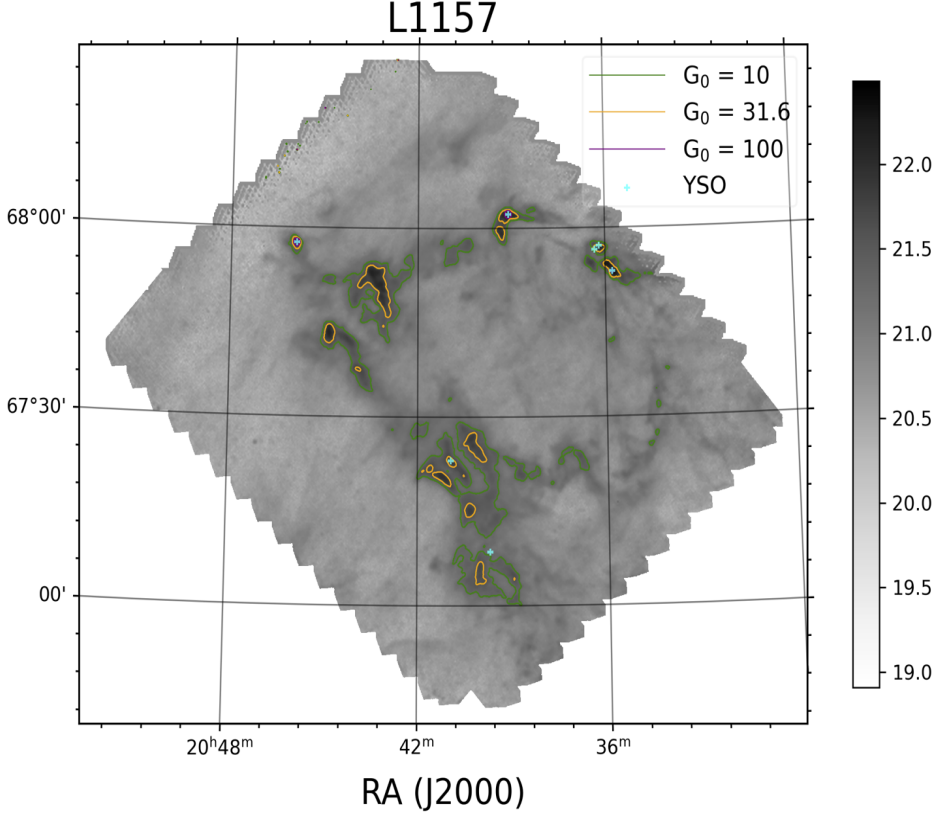


Figure 7. Contours of UV intensity overlaid on H_2 column density map of the L1157 region. The labels of the figure are the same as that in Fig. 3.

A.6. *Musca*

With distance of ~ 200 pc, the Musca cloud is a 10.5 pc long filament with low-mass star formation (Cox et al. 2016). The mass of Musca molecular cloud is about $335 M_\odot$ (Evans et al. 2014). There are no massive stars in this region. It is clear from Fig. 20, UV intensity increases in some dense regions.

A.7. ρ Oph

With distance of 125 pc (Evans et al. 2014), the ρ Oph molecular cloud is one of the most conspicuous nearby regions where low and intermediate-mass star formation is taking place (Wilking 1992). The total mass of the ρ Oph cloud is about $3128 M_\odot$, one third of which is dense gas. The ρ Oph cloud consists of two massive, centrally condensed cores, L1688 and L1689 (Loren 1989). Being different from L1689 with little star formation activity, L1688 harbors a rich cluster of YSOs at various evolutionary stages and is distinguished by high star-formation efficiency (Wilking & Lada 1983). Two OB stars (HD 147889 and ρ Oph A) are found in this region.

The UV radiation distribution of ρ Oph cloud is shown in Fig. 21. A strong correlation between UV intensity and star distribution was found. The UV intensity G_0 can exceed 1000 in dense gas region and regions around OB stars.

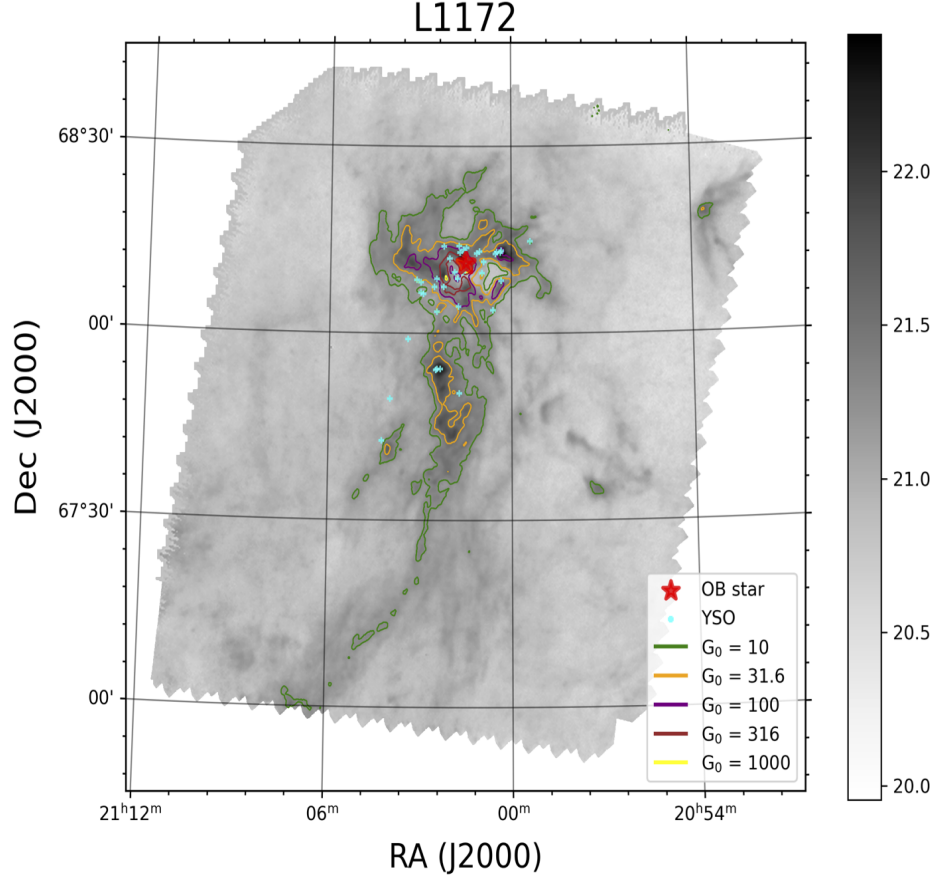


Figure 8. Contours of UV intensity overlaid on H_2 column density map of the L1172 region. The labels of the figure are the same as that in Fig. 3. The red star implies the location of OB star in this region.

A.8. *Perseus*

The Perseus molecular clouds is ~ 250 pc away with sky coverage of ~ 10 deg². It is a low and intermediate-mass star-forming region. The total mass of the Perseus molecular cloud is about $6586 M_\odot$, one third of which is dense gas (Evans et al. 2014). As shown in Fig. 22, UV radiation field correlates with the locations of OB stars and YSOs in this region.

A.9. *Pipe*

The Pipe Nebula has a distance of ~ 145 pc (Alves & Franco 2007). Composed of an elongated dark cloud with length of 18 pc, the Pipe Nebula is one of the closest star-forming regions. The Pipe Nebula is an ideal target for investigating core formation. The mass of the Pipe nebula is about $1.7 \times 10^4 M_\odot$ (Lombardi et al. 2006). A few identified YSOs were found in this region (Peretto et al. 2012). As shown in Fig. 23, the UV intensity is very low ($G_0 < 31.6$) toward most region of this molecular complex.

A.10. *Serpens*

The Serpens star-forming region located at ~ 429 pc was covered in ~ 15 deg² by HGBS (Evans et al. 2014). Its total mass is $\sim 6583 M_\odot$, two thirds of which is dense gas (Evans et al. 2014). About 81 percent of the prestellar cores are found in the filamentary structure of Serpens (Fiorellino et al. 2021). Serpens is confirmed to be a low-mass and active star-forming region at a young age. As shown in Fig. 24, lots of YSOs and an OB star were found in this region.

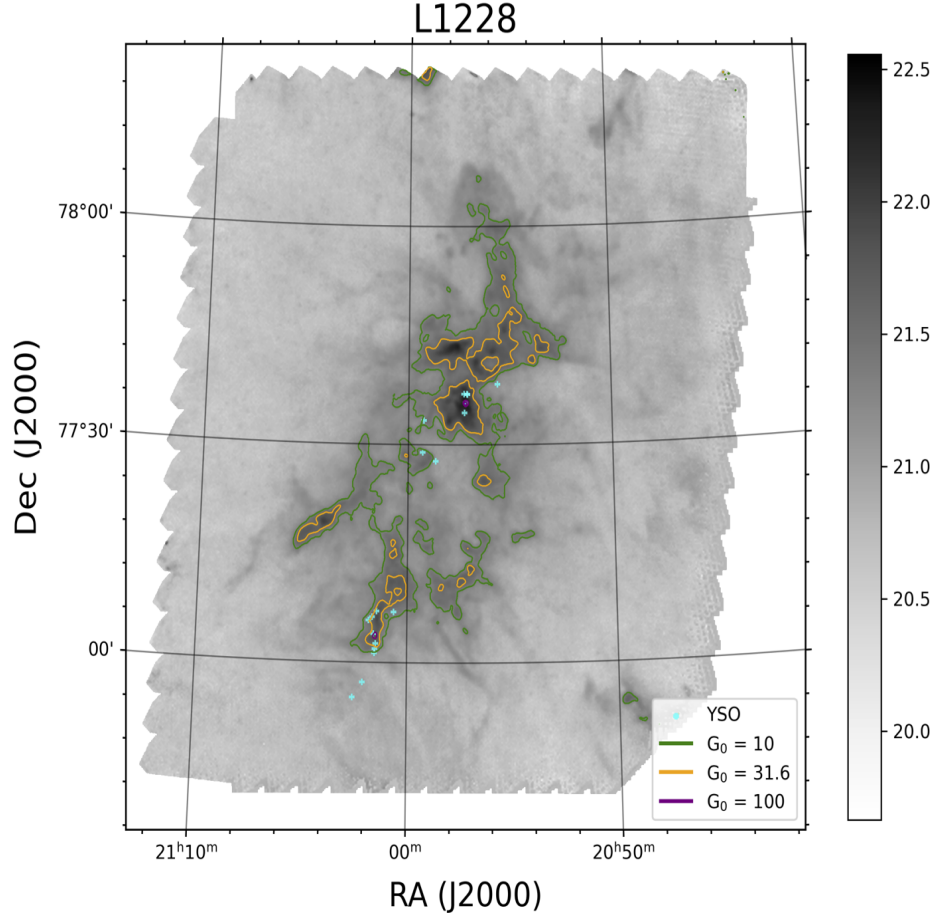


Figure 9. Contours of UV intensity overlaid on H₂ column density map of the L1228 region. The labels of the figure are the same as that in Fig. 3.

A.11. *Taurus*

The distance of Taurus cloud to our solar system is about 140 pc (Palmeirim et al. 2013). The total mass of Taurus molecular cloud is about $2\text{--}4 \times 10^4 M_{\odot}$, ten percent of which is dense gas (Evans et al. 2014). HGBS covered about 52 deg² of this region (Kirk et al. 2013). No OB stars was found in the Taurus molecular cloud. As shown in Fig. 25, the UV radiation intensity correlates with the distribution of dense gas.

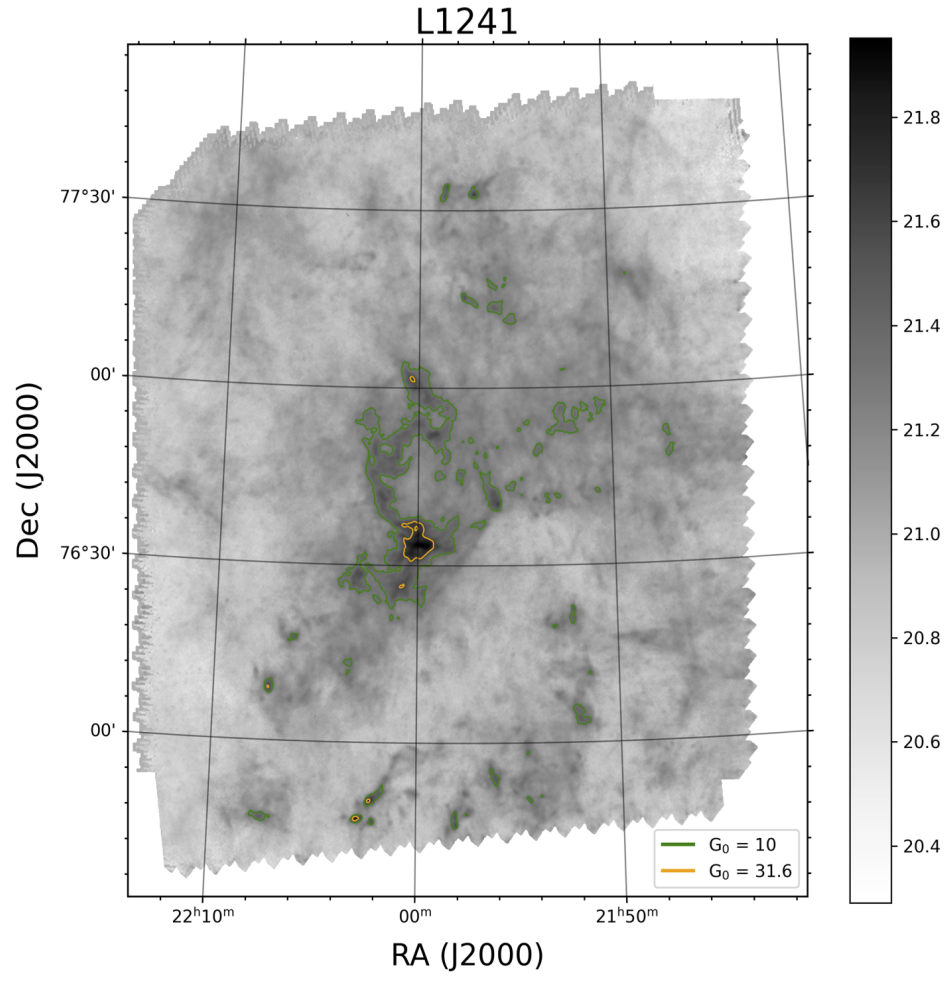


Figure 10. Contours of UV intensity overlaid on H₂ column density map of the L1241 region. The labels of the figure are the same as that in Fig. 3. There is no YSOs nor OB star in this region.

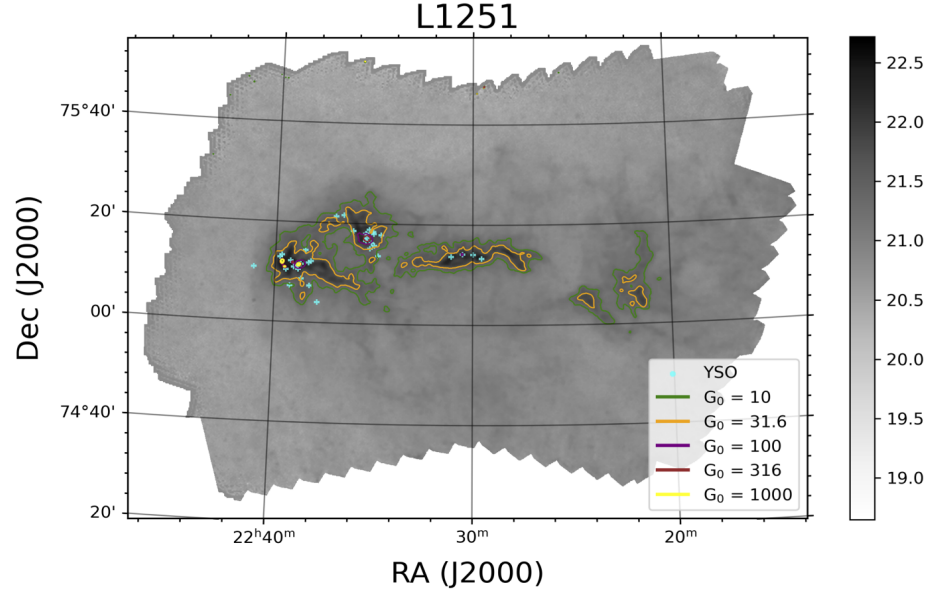


Figure 11. Contours of UV intensity overlaid on H₂ column density map of the L1251 region. The labels of the figure are the same as that in Fig. 3.

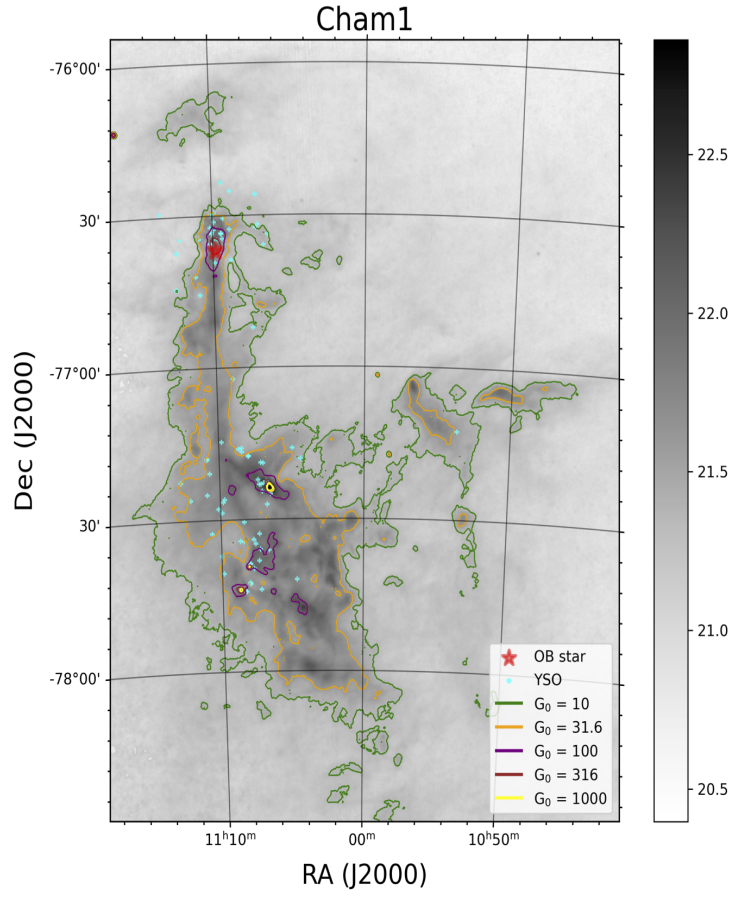


Figure 12. Contours of UV intensity overlaid on H_2 column density map of the Cham I region. The labels of the figure are the same as that in Fig. 8.

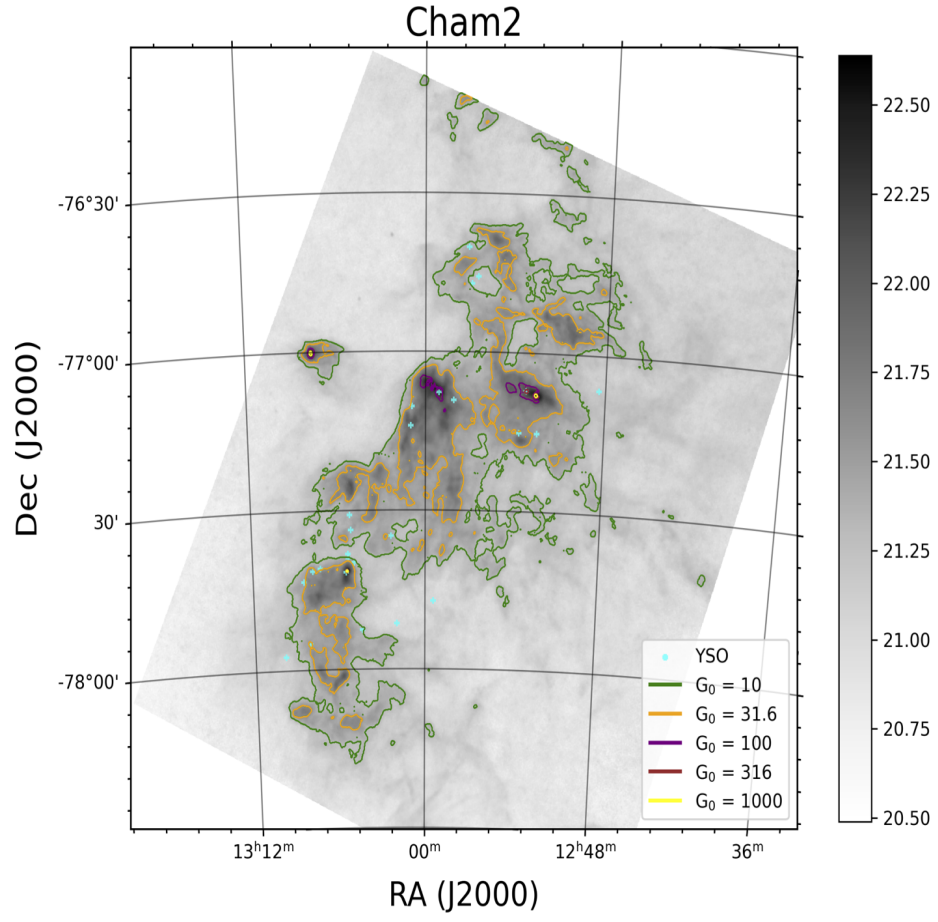


Figure 13. Contours of UV intensity overlaid on H_2 column density map of the Cham II region. The labels of the figure are the same as that in Fig. 3.

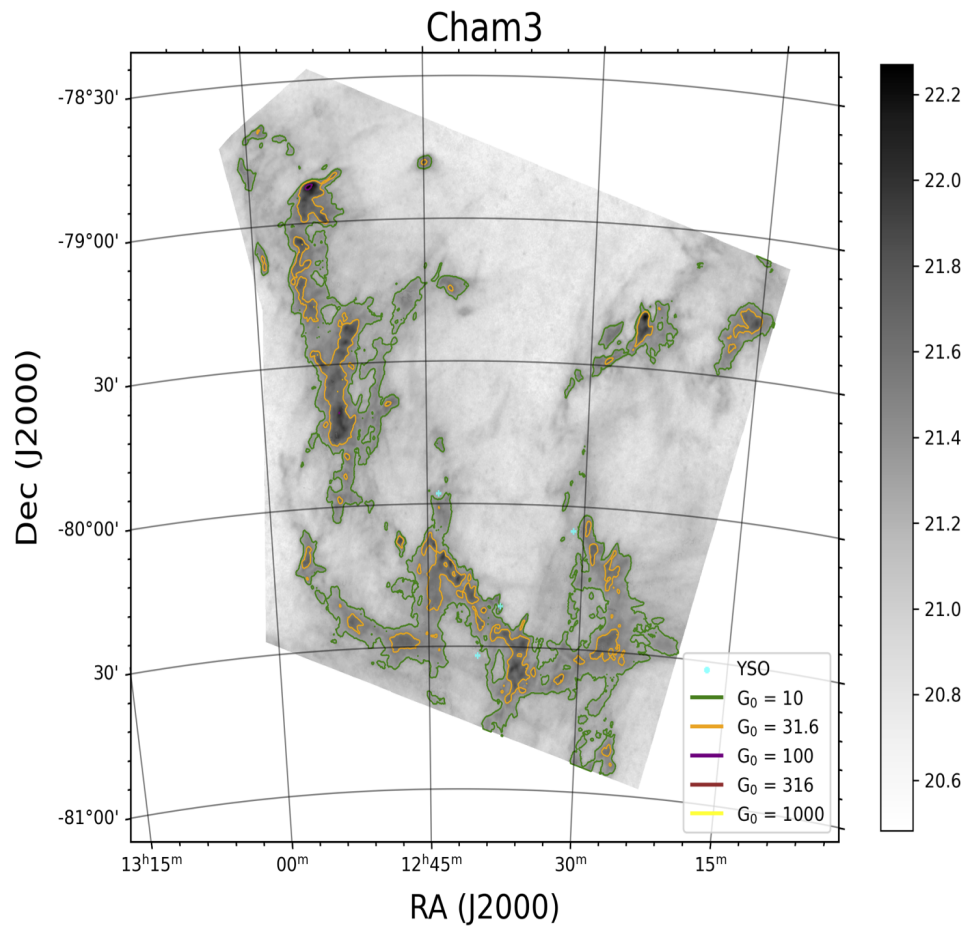


Figure 14. Contours of UV intensity overlaid on H_2 column density map of the Cham III region. The labels of the figure are the same as that in Fig. 3.

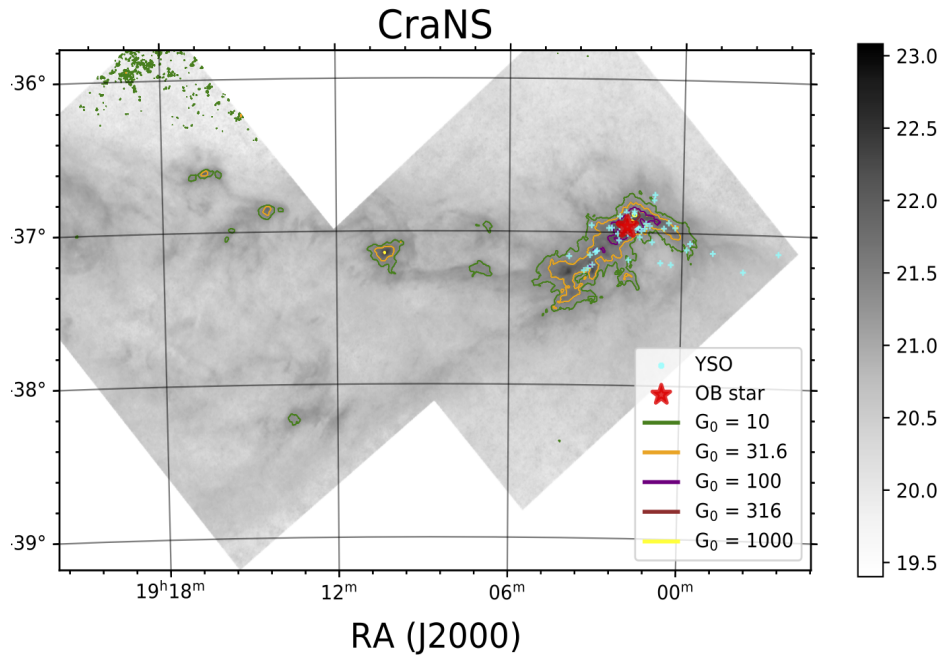


Figure 15. Contours of UV intensity overlaid on H_2 column density map of the CraNS region. The labels of the figure are the same as that in Fig. 3.

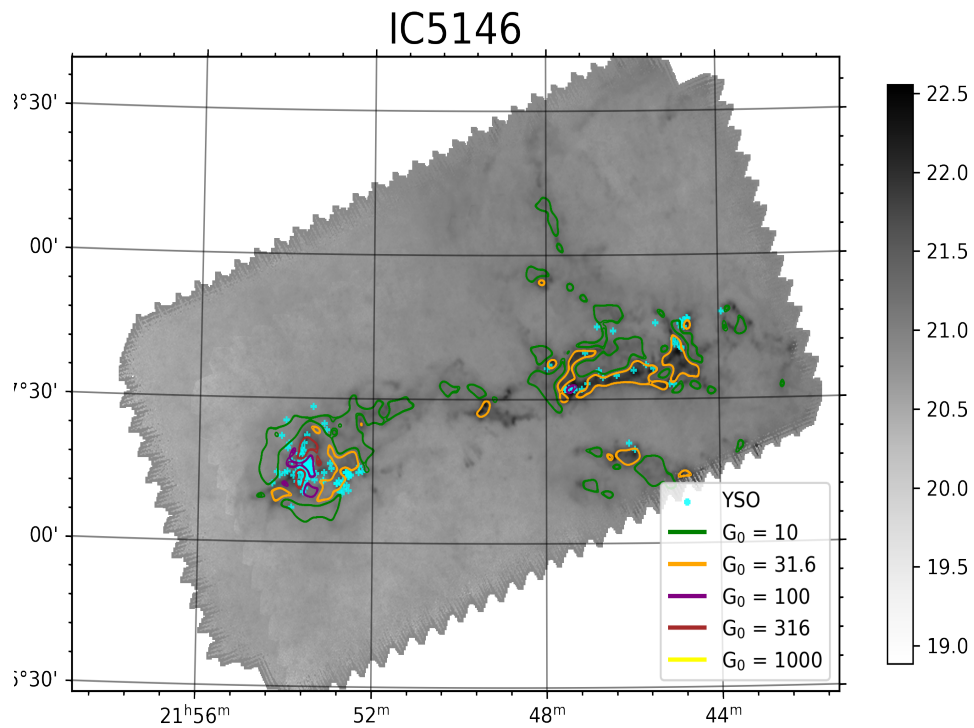


Figure 16. Contours of UV intensity overlaid on H_2 column density map of the IC 5146 region. The labels of the figure are the same as that in Fig. 3.

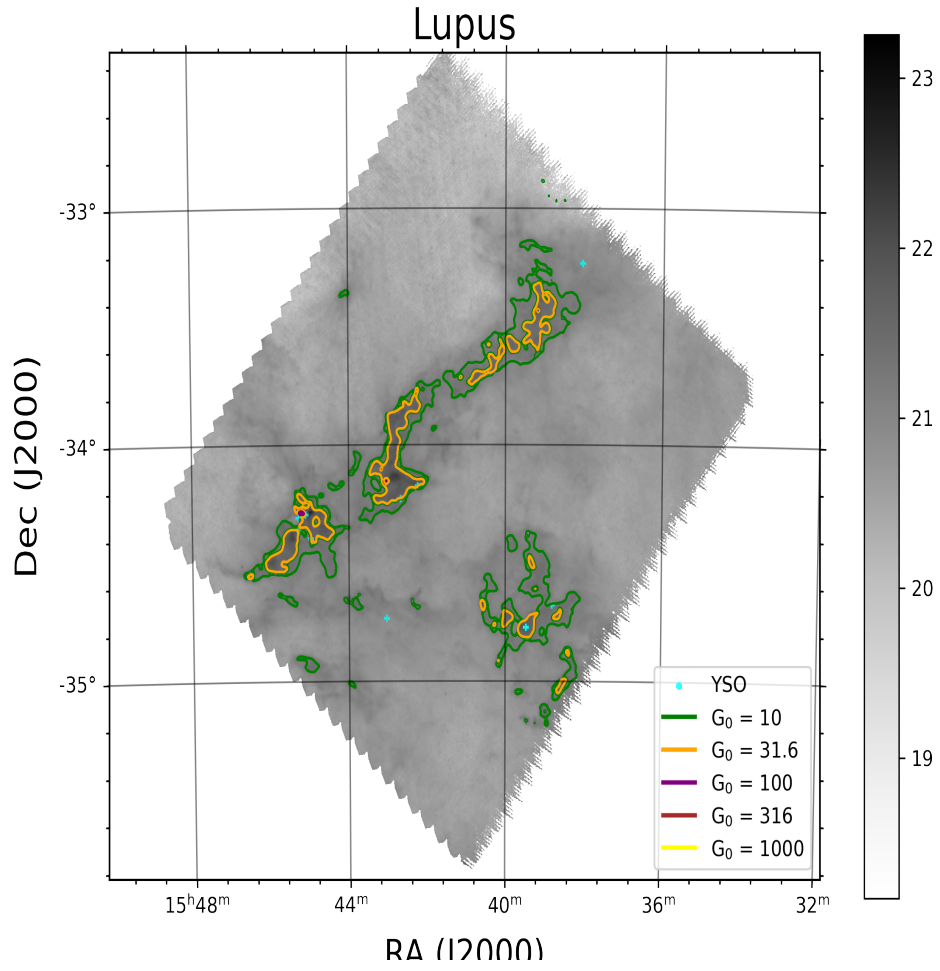


Figure 17. Contours of UV intensity overlaid on H_2 column density map of the Lupus I region. The labels of the figure are the same as that in Fig. 3.

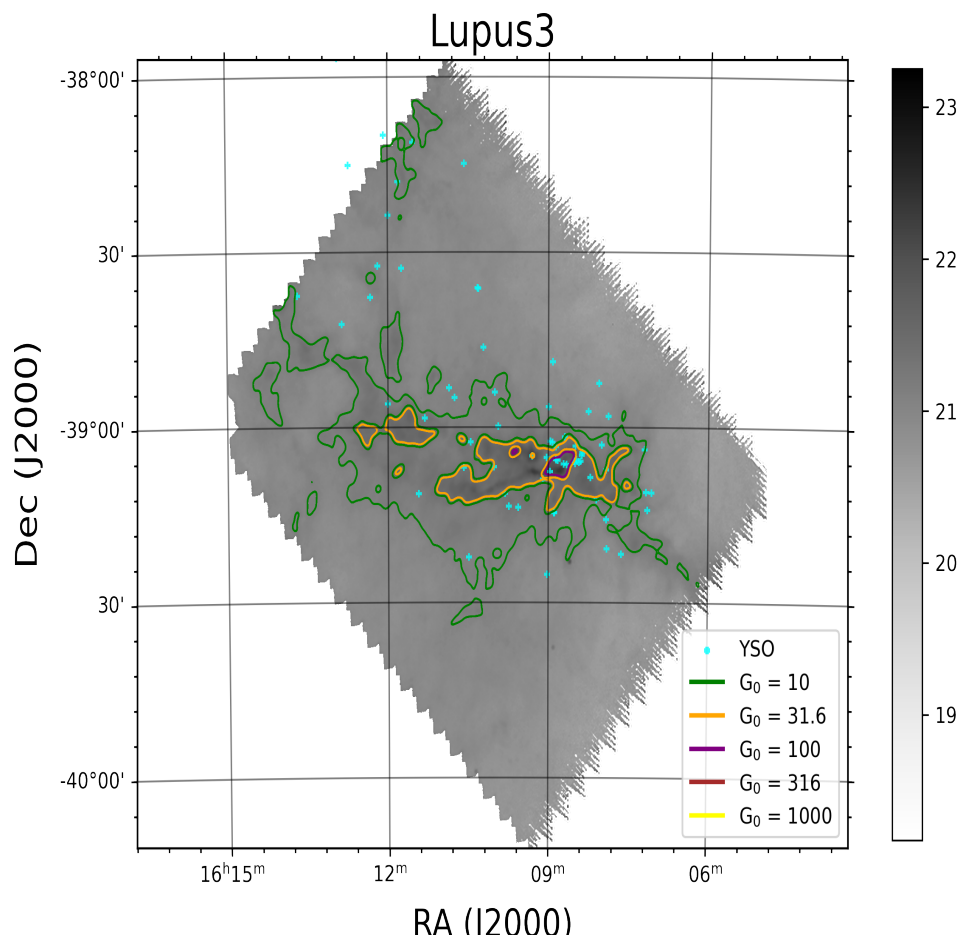


Figure 18. Contours of UV intensity overlaid on H_2 column density map of the Lupus III region. The labels of the figure are the same as that in Fig. 3.

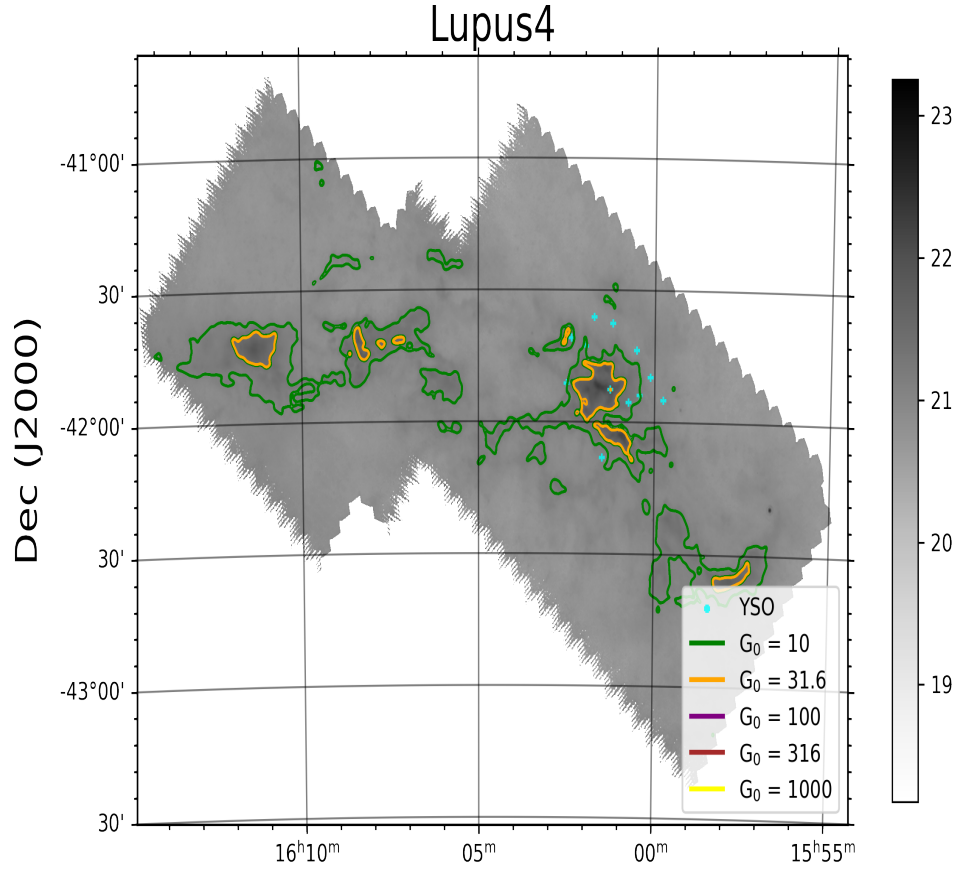


Figure 19. Contours of UV intensity overlaid on H_2 column density map of the Lupus IV region. The labels of the figure are the same as that in Fig. 3.

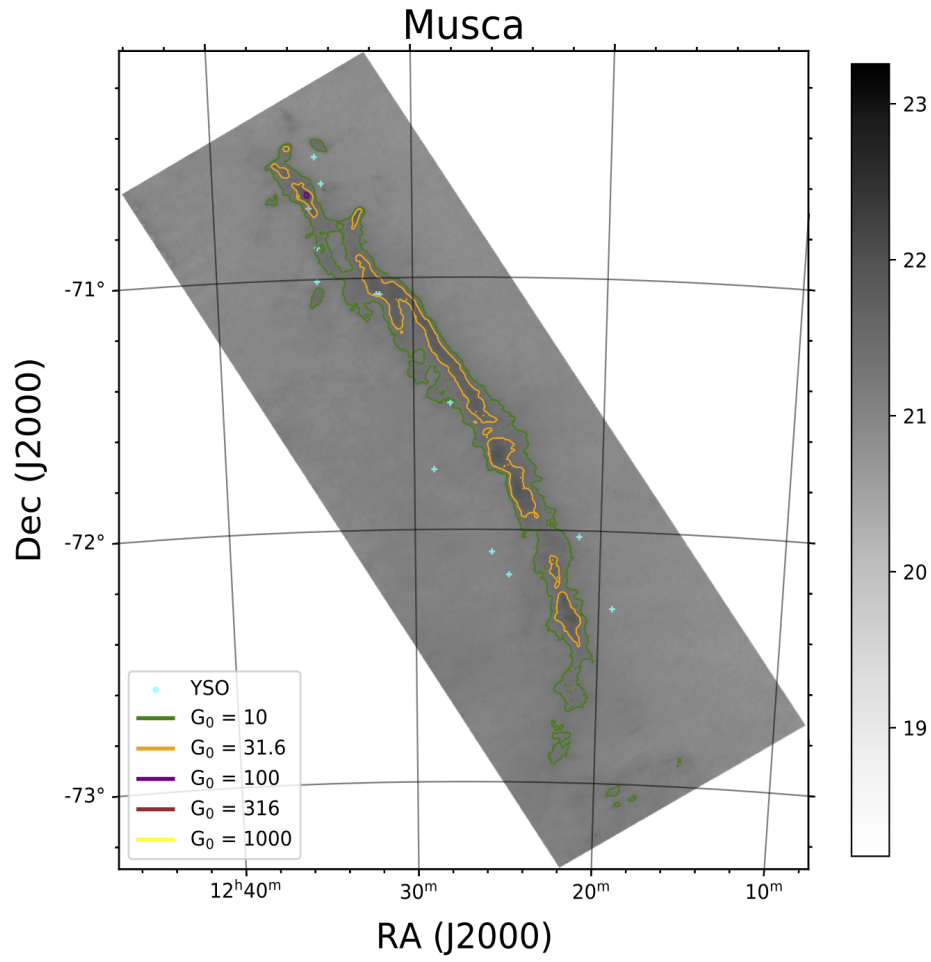


Figure 20. Contours of UV intensity overlaid on H₂ column density map of the Musca region. The labels of the figure are the same as that in Fig. 3.

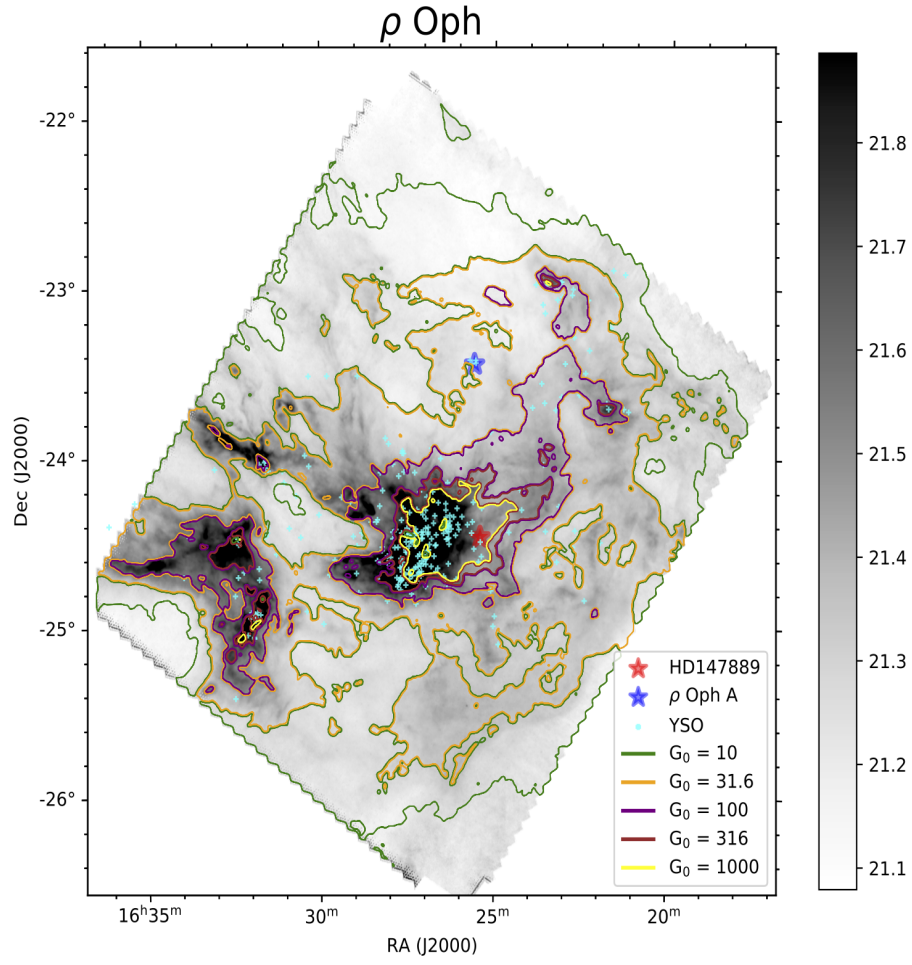


Figure 21. Contours of UV intensity overlaid on H_2 column density map of the ρ Oph region. The labels of the figure are the same as that in Fig. 8.

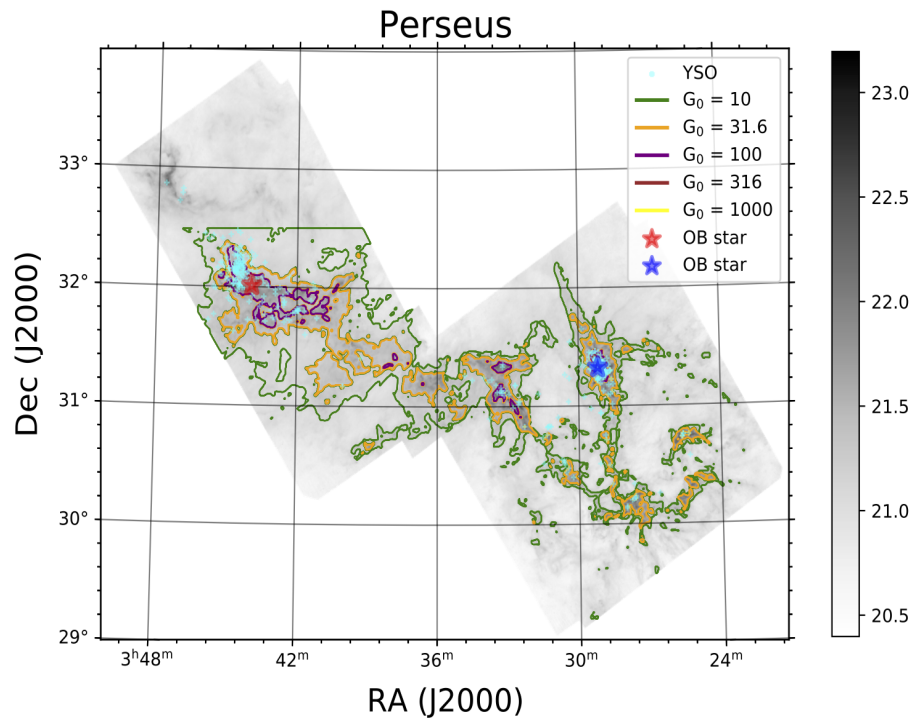


Figure 22. Contours of UV intensity overlaid on H_2 column density map of the Perseus region. The labels of the figure are the same as that in Fig. 8.

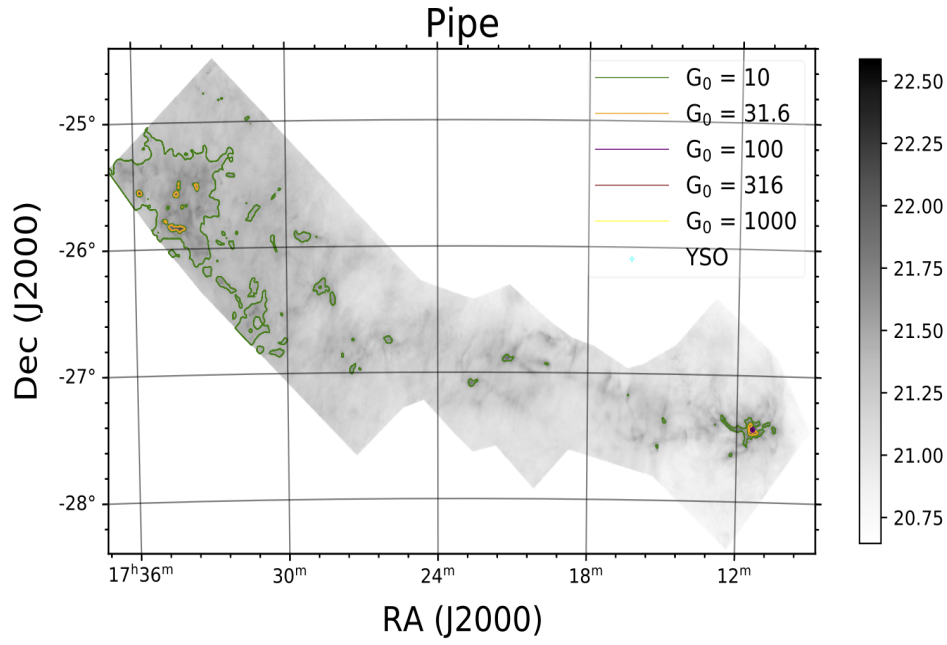


Figure 23. Contours of UV intensity overlaid on H_2 column density map of the Pipe region. The labels of the figure are the same as that in Fig. 3.

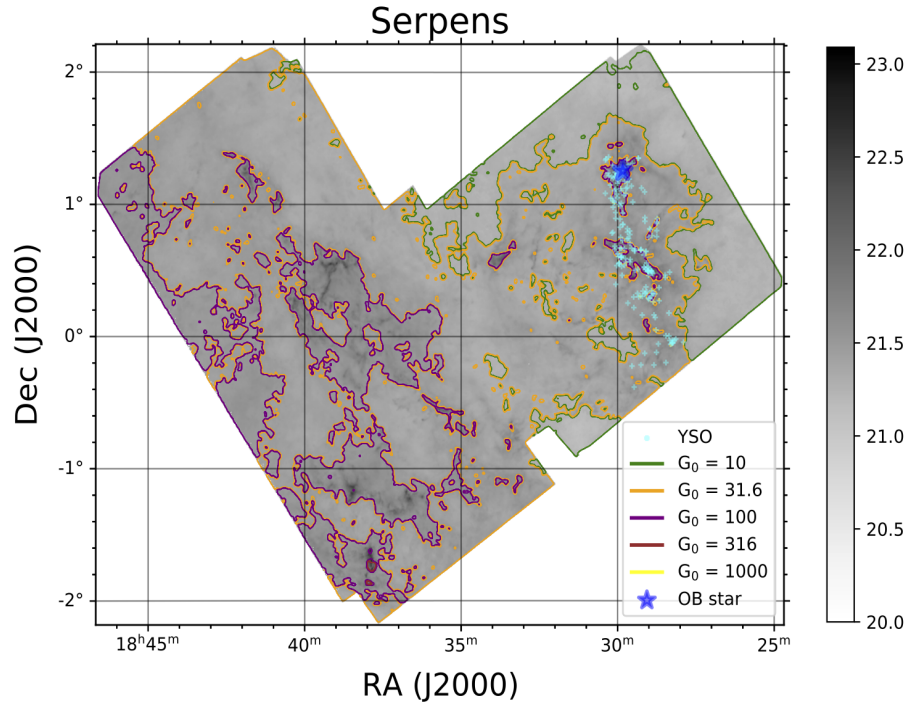


Figure 24. Contours of UV intensity overlaid on H_2 column density map of the Serpens region. The labels of the figure are the same as that in Fig. 8

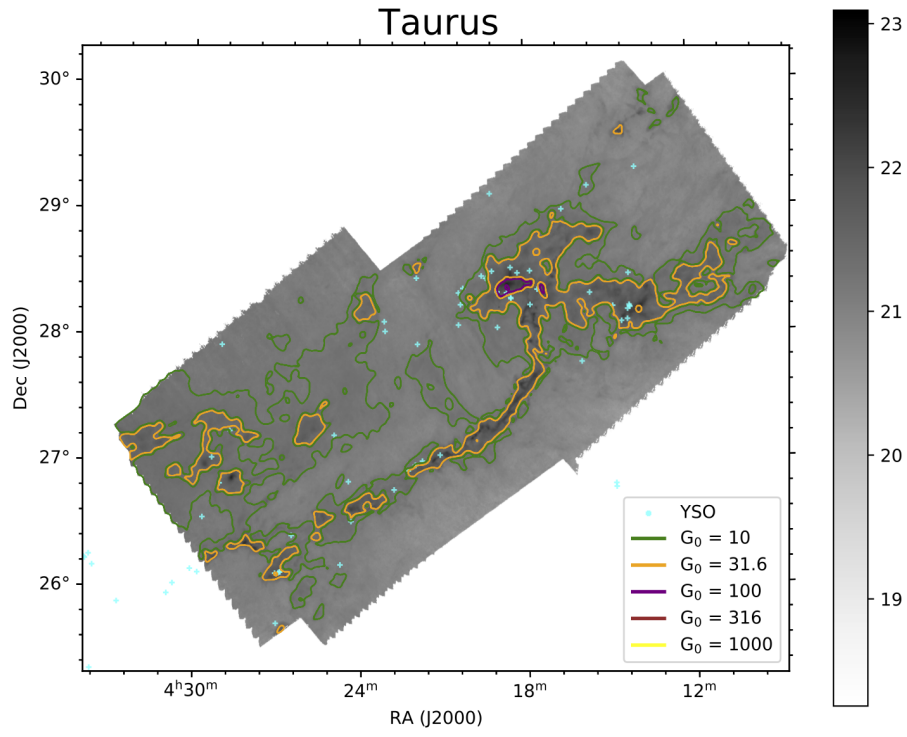


Figure 25. Contours of UV intensity overlaid on H_2 column density map of the Taurus region. The labels of the figure are the same as that in Fig. 3.